communications physics

Article

https://doi.org/10.1038/s42005-024-01918-w

Surface-specific thermal spin-depolarization on the half-metallic Heusler films

Kazuki Sumida [1,7] ✉, Masaaki Kakoki[2,7], Yuya Sakuraba [3], Keisuke Masuda [3], Kazuki Goto[3], Takashi Kono[4], Koji Miyamoto [1], Yoshio Miura[3], Kazuhiro Hono[3], Taichi Okuda [1,5,6] & Akio Kimura [2,4,5,6] ✉

Half-metallic ferromagnets exhibit a perfect spin-polarization at the Fermi energy. Among many candidates, Co_2MnSi Heusler alloy is the most investigated material due to its half-metallic nature and high Curie temperature (T_C). Magnetic junction devices using Co_2MnSi show remarkable performance at low temperatures. However, the performance is significantly degraded at room temperature, which requires a detailed understanding of the temperature-dependent electronic structure of Co_2MnSi films. Here, using surface-sensitive spin- and angle-resolved photoelectron spectroscopy combined with first-principles calculations, we verify the temperature- and momentum-dependent spin-polarization of Co_2MnSi thin-film. The recorded spin-polarization reaches ~ 60-75% at 50 K, while it reduces ~ 30-50% at 300 K. The observed surface-specific spin-depolarization behavior can be described by the thermally excited magnon model even well below T_C, and we conclude that the spin-fluctuation is markedly enhanced on its surface. Our findings provide insights into the temperature-dependent electronic structure of half-metallic Heusler films, which could have significant implications for future spintronic applications.

Heusler alloys are typical intermetallic compounds described as X_2YZ, where X and Y sites mainly comprise transition metal elements, while the Z site consists of main block elements such as Al, Si, Ga, and Ge. The paramount characteristic of the Heusler alloys lies in their ability to manifest diverse properties, including half-metallicity, shape memory effect, thermoelectric effect, magneto-caloric effect, superconductivity, catalytic property, and topological property by changing the constituent elements[1–6]. Several Co- and Mn-based Heusler alloys, e.g., Co_2MnSi, Co_2MnGe, and Mn_2VAl, are theoretically predicted to possess a half-metallic electronic structure, where one spin channel exhibits metallic feature while the other behaves as a semiconductor[7–10]. Owing to a perfect spin-polarization at the Fermi level (E_F) and a very high Curie temperature (T_C) exceeding room temperature, they are considered promising materials for spintronic applications, particularly in magnetic sensing and recording devices. Among them, Co_2MnSi stands out as one of the most extensively studied half-metallic ferromagnets from both fundamental and practical perspectives. Over the past two decades, there has been notable progress in enhancing the performance of tunnel magnetoresistance (TMR) and giant magnetoresistance (GMR) devices using Co_2MnSi as a ferromagnetic electrode[11–17]. For instance, epitaxial $Co_2MnSi/MgO/Co_2MnSi$ magnetic tunnel junctions have achieved a TMR ratio exceeding 2000% at 4.2 K[17]. However, the TMR ratio decreases substantially by a factor of six at 290 K (335%), despite being well below T_C of 985 K. Similar performance degradation at room temperature has also been found in GMR devices[16]. These observations suggest that the electronic structure, particularly spin-polarization, in the bulk, surface, or interface regions of Co_2MnSi thin films undergoes significant changes with temperature.

Theoretical calculations have proposed several spin-depolarization mechanisms of Co_2MnSi at finite temperatures. A combination of density-functional theory and dynamical mean-field theory predicts the formation

[1]Research Institute for Synchrotron Radiation Science, Hiroshima University, 2-313 Kagamiyama, Higashi-Hiroshima, 739-0046, Japan. [2]Graduate School of Advanced Science and Engineering, Hiroshima University, 1-3-1 Kagamiyama, Higashi-Hiroshima, 739-8526, Japan. [3]Research Center for Magnetic and Spintronic Materials, National Institute for Materials Science, Sengen 1-2-1, Tsukuba, 305-0047, Japan. [4]Graduate School of Science, Hiroshima University, 1-3-1 Kagamiyama, Higashi-Hiroshima, 739-8526, Japan. [5]International Institute for Sustainability with Knotted Chiral Meta Matter (WPI-SKCM2), 1-3-1 Kagamiyama, Higashi-Hiroshima, 739-8526, Japan. [6]Research Institute for Semiconductor Engineering, 1-4-2 Kagamiyama, Higashi-Hiroshima, 739-8527, Japan. [7]These authors contributed equally: Kazuki Sumida, Masaaki Kakoki. ✉e-mail: sumidak1126@hiroshima-u.ac.jp; akiok@hiroshima-u.ac.jp

of non-quasiparticle states in the bulk electronic structure[18]. Spin-flip scattering through interface states induced by magnetic excitations is also proposed[19,20]. Specifically, it is argued that the Co-terminated interfaces between Co_2MnSi and MgO are thermodynamically unstable[21,22]. In addition, the effective exchange constant of the topmost Co atom was calculated and found to be extremely reduced compared to that of the bulk, indicating that thermal spin fluctuations are enhanced on the surface of Co_2MnSi at finite temperatures[23]. More recently, the influence of magnon on the bulk electronic structure of Co_2MnSi has been investigated using disordered local-moment methods, which treat spin fluctuations as local moments within a mean-field approximation[24,25]. As a consequence, it is predicted that the magnon excitations eliminate half-metallicity at room temperature.

From an experimental standpoint, the spin-polarized electronic structure of Co_2MnSi thin-film has been investigated using surface-sensitive low-photon-energy and bulk-sensitive high-photon-energy spin-resolved photoelectron spectroscopy measurements in the momentum-integrated mode[26–32]. However, the reported magnitudes of spin polarization varied significantly. Former works reported unexpectedly low spin-polarization, approximately 10–30% at room temperature, by employing a vacuum ultraviolet (VUV) synchrotron radiation with photon energy ($h\nu$) of 70 eV[26] and the fourth harmonic of Ti:Sapphire laser at 5.9 eV[27]. Conversely, nearly a perfect spin-polarization of 93% was observed by the He discharge lamp at 21.2 eV[28]. In 2016, a systematic investigation of spin-polarization of Co_2MnSi thin films with different atomic compositions, utilizing VUV synchrotron radiation, revealed that the value at E_F is relatively small (~25%) for stoichiometric compositions but markedly increases to ~75% for Mn-rich compositions by controlling the energy position of the weakly exchange-split surface state[29]. Furthermore, ex situ bulk-sensitive spin-resolved photoemission spectroscopy has recently been conducted on MgO-coated nearly stoichiometric Co_2MnSi thin-film at 21 and 300 K using hard X-ray synchrotron radiation at 5950 eV[32]. According to this work, the spin-polarization in the bulk region reached approximately 90% and did not show a pronounced temperature dependence at E_F. In fact, this result is inconsistent with the temperature-dependent behavior of the TMR and GMR devices and indicates that the electronic structure near the surface/interface region of Co_2MnSi, rather than in bulk, may play a crucial role in the performance degradation at room temperature.

To address the aforementioned inconsistency, in this work, we performed surface-sensitive spin- and angle-resolved photoelectron spectroscopy (SARPES) utilizing a high-efficiency very low energy electron diffraction (VLEED) type spin-polarimeter on Co_2MnSi films at various temperatures and compared the results with surface slab calculations. Our VLEED-based SARPES instrument combined with synchrotron radiation not only reveals the complete electronic structure of Co_2MnSi in energy, momentum, and spin-resolved manners but also allows us to track the detailed temperature evolution of spin-polarization near E_F with a resolution an order of magnitude higher than previous works. We experimentally determined the temperature and momentum-dependent spin-polarization of Co_2MnSi films and demonstrated a dramatic change on its surface. The surface-specific spin-depolarization is well explained by the extended Bloch $T^{3/2}$ model (Shang model)[33], indicating that the spin fluctuation due to thermally excited magnons is drastically enhanced at the surface of Co_2MnSi films.

Results and discussion

Characterization of the structural, magnetic, and electronic properties of the fabricated thin-film

A crystallographic unit cell of the $L2_1$-ordered Heusler alloy Co_2MnSi, which belongs to the cubic $Fm\bar{3}m$ space group, is shown in Fig. 1a. We fabricated a 30-nm-thick Co_2MnSi epitaxial thin-film on MgO(001) substrate with buffer layers of Cr and Ag to increase the crystallinity and flatness. Figure 1b shows the X-ray diffraction (XRD) profiles of the fabricated sample taken by setting the scattering vector to [001] (main figure) and [111] (left inset) directions. We clearly see 002 and 111 superlattice peaks originating from $B2$ and $L2_1$ ordering, respectively. These results signify the epitaxial growth of the $L2_1$-ordered Co_2MnSi film. The surface morphology of the sample was measured by atomic force microscopy (AFM). The root-mean-square roughness, estimated at a scan size of 2 μm × 2 μm (right inset, Fig. 1b), was found to be ~0.15 nm, which is notably flatter than the previously reported values[34–36]. Magnetization curves recorded at 50 and 300 K with an external field applied to the [110] direction are displayed in Fig. 1c. Owing to the magnetic shape anisotropy of the film, an almost temperature-independent large in-plane remanent magnetization (M_r) was observed. These characteristics allow us to perform the SARPES measurements at zero-field with various temperatures.

In order to experimentally verify the band structure of Co_2MnSi film, we first performed in situ ARPES measurement at room temperature with surface-sensitive VUV synchrotron excitation. Figure 1e shows the observed band structure along the Γ–X–Γ_{2nd} line utilizing p-polarized 70 eV incidence photon, which corresponds to the k_z ~0 plane of the bulk Brillouin zone (Fig. 1d and S4 in the Supplementary Information). Around the X point, we found that a very steep electron band crosses E_F (labeled A). Bands with strong photoelectron intensities can be seen in a wide momentum region around $E - E_F = -1.0$ eV (labeled B). Moreover, although it is not clear in the first Brillouin zone, probably due to the matrix element effect, an upward convex band is identified around the Γ_{2nd} point (labeled C). To enhance the visibility of the bands, the Laplacian-filtered ARPES image is displayed in Fig. 1f. After the Laplacian-filtering, some weak intensity bands are clearly visualized. Mostly non-dispersive bands are found around −0.1 (labeled SS) and −0.6 eV (labeled D). These experimentally observed features are qualitatively reproduced by the bulk band calculations shown in Fig. 1g, except for the non-dispersive band SS just below E_F. By comparing the ARPES results and the calculations, we identify that the experimentally observed bands A and B (C and D) are composed of majority-spin (minority-spin) states. Based on the calculation, the band A comprises two bands with Δ_1 and Δ_5 symmetries. However, these bands are mostly smeared, making it difficult to separate them in the experiment. The unexpected band SS seen in the surface-sensitive VUV-ARPES might be attributed to the surface band structure (see also Fig. S5 in the Supplementary Information), which will be discussed later.

Temperature-dependent VUV-ARPES measurements around X point

To clarify the temperature evolution of the bands, we next cooled down the sample. Since the bulk band intersecting E_F was only observed around the X point, we focus here on the temperature dependence of the electron-band A. Figure 2a shows the magnified ARPES images around X point recorded at 300, 250, 200, 150, 100, and 50 K. In fact, no noticeable changes, such as the band shift or the emergence of additional bands, are observed in this temperature range. To scrutinize the detailed differences, Fig. 2b shows the peak fitting results of the ARPES images. The peak positions were determined by energy distribution curves (EDCs) and momentum distribution curves (MDCs) at each temperature. The black curve represents the fitted result with a parabolic function. Based on the fitting results, the Fermi momentum (k_F), Fermi velocity (v_F), and effective mass (m^*) of our Co_2MnSi film were determined to be 0.80 $Å^{-1}$, 3.94×10^5 m s^{-1}, and 0.79 times the bare electron mass (m_e), respectively. Importantly, these band-structure-related parameters show no distinct temperature dependence within the experimental resolutions.

Figure 2c, d shows the EDCs at k_F and the X point recorded at temperatures ranging from 300 to 50 K. At k_F, a clear metallic edge mainly originating from the majority-spin electron-band A is observed (Fig. 2c). Similarly, we also find a metallic feature at the X point indicated by a blue shaded area (Fig. 2d). However, the bulk band calculation predicts that there are no states at E_F at the X point (Fig. 1g). The emergence of the unexpected density of states (DOS) at the X point is attributed to the non-dispersive SS band shown in Fig. 1f. Overall, neither band A nor SS near E_F shows significant temperature dependence. These findings are consistent with previously reported bulk-sensitive angle-integrated hard X-ray photoelectron spectroscopy results[32,37].

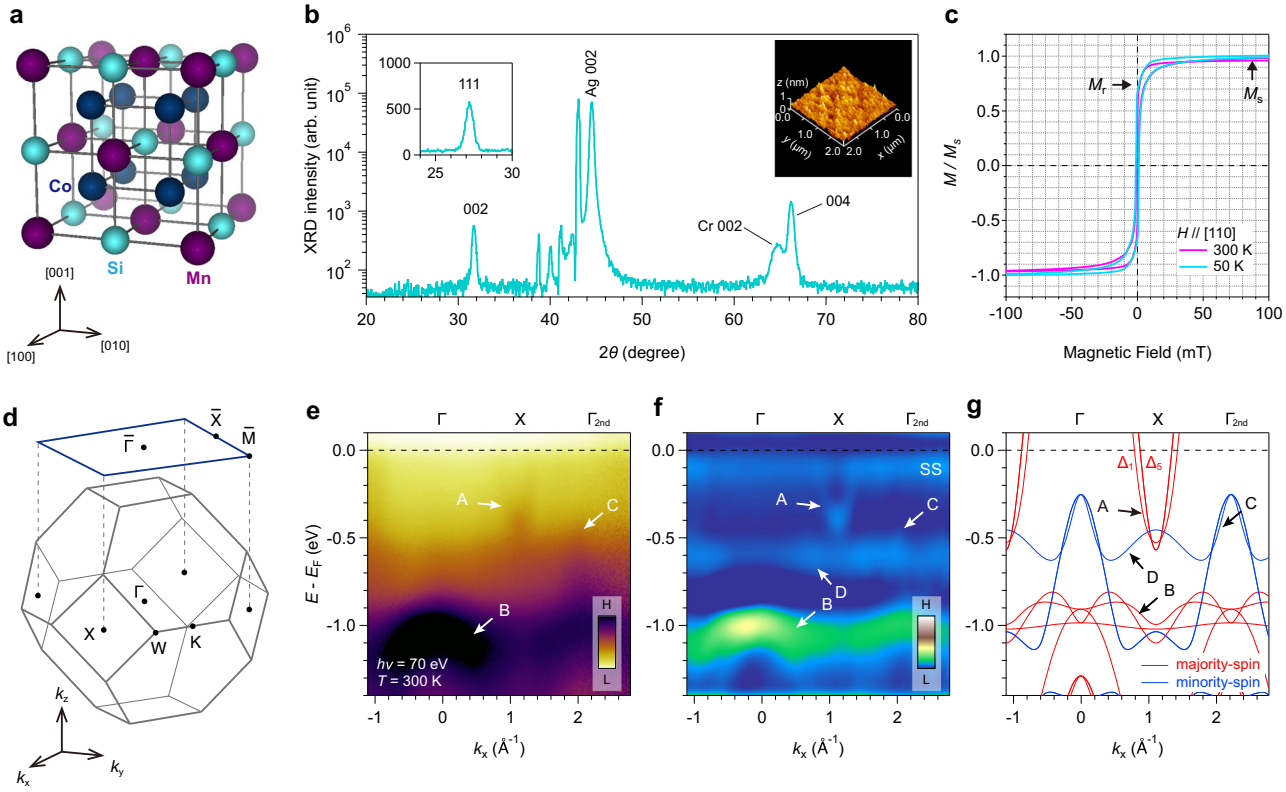

Fig. 1 | Structural, magnetic, and electronic properties of the fabricated thin-film. **a** Schematic of the $L2_1$-ordered Co_2MnSi crystal structure. **b** XRD pattern taken at [001] (normal) direction. The unlabeled peaks originate from the MgO substrate. The left inset shows an XRD pattern taken at [111] direction. The right inset shows an AFM image of the fabricated sample in a scan size of 2 μm × 2 μm. **c** Magnetic-field-dependent magnetization at 300 and 50 K. The external magnetic field was applied along [110] direction. Magnetization was normalized by saturation magnetization (M_s) at 50 K. **d** Bulk and surface Brillouin zones of Co_2MnSi. **e** Observed band structure of Co_2MnSi film along the Γ–X–$Γ_{2nd}$ line recorded at 70 eV with *p*-polarized light at 300 K. Colors show the photoelectron intensity. **f** Laplacian-filtered image of (**e**). **g** Calculated bulk band structure of Co_2MnSi. Red and blue represent majority- and minority-spin bands, respectively.

Temperature-dependent spin- and momentum-resolved photoelectron spectra

To gain deeper insight into the temperature evolution of the electronic structure of Co_2MnSi film, we performed temperature-dependent spin- and momentum-resolved measurements. Figure 3a, b shows the observed spin-resolved EDCs and spin-polarization around k_F and X point recorded at 300, 250, 200, 150, 100, and 50 K. For both momenta, the majority-spin states are dominant (positively spin-polarized) over the entire energy region, and the observed spectral shapes are similar to the calculated momentum-integrated bulk DOS (Fig. 3c). However, in sharp contrast to the bulk calculations, the metallic features are recognized at E_F in the minority-spin channel at all temperatures (indicated by blue arrows in Fig. 3a, b), signifying that an in-gap state exists and destroys the half-metallicity on the surface. More importantly, we experimentally verified that the spin-polarization increases with decreasing temperature, although the spin-integrated spectral shape remains unchanged in this temperature region (Fig. 2c, d). This means that the photoelectron intensity at the majority-spin (minority-spin) channel increases (decreases) with decreasing temperature. The recorded spin-polarization around E_F at 50 K (300 K) reaches ~75% (~50%) at the X point, while it is ~60% (~30%) at k_F. At all temperatures, the spin-polarization at the X point is higher than that at k_F (lower panels of Fig. 3a, b).

Figure 3d summarizes the temperature- and momentum-dependent spin-polarization at E_F. We here apply the Shang model[33] (extended Bloch $T^{3/2}$ model[38,39]) to explain the spin-depolarization mechanism. The model accounts for the thermal spin fluctuation due to low-energy long-range spin waves (magnons) at finite temperatures below T_C and can be described as $P(T) = P_0(1 - \alpha T^{3/2})$, where P_0 and α denote the estimated spin-polarization at 0 K and the material-dependent constant, respectively. The theoretical curves nicely trace the experimentally obtained spin-polarization at both momenta (see blue-green solid curves) and give $P_0(k_F) = 61\%$, $P_0(X) = 80\%$, $\alpha(k_F) = 1.15 \times 10^{-4}$, and $\alpha(X) = 8.30 \times 10^{-5}$. The overall agreement indicates that the observed spin-depolarization behavior can be explained by the thermally excited magnon model even well below T_C. In Fig. 3d, we also plot the temperature-dependent spin-polarization observed by the hard X-ray spin-resolved photoelectron spectroscopy (HAX-SPES) (red markers)[32] and the magnetization obtained by macroscopic magnetometry measurements (orange markers). Surprisingly, the coefficients α obtained using these methods are found to be one or two orders of magnitude smaller than that of VUV-SARPES. This significant difference is probably attributed to the bulk/surface sensitivity of the experimental methods. The inelastic mean free path of VUV-SARPES (70 eV) is about 5 Å based on the so-called universal curve[40]. On the other hand, it is ~7 nm for HAX-SPES (5950 eV)[32], which means that HAX-SPES can detect spin-polarization from a region more than ten times deeper than VUV. In the case of magnetometry measurements, since the magnetization signal is proportional to the volume fraction, the bulk contribution is dominant rather than the surface contribution. Considering all the experimental findings, we conclude that the temperature-dependence of the surface electronic and magnetic properties of Co_2MnSi film are quite different from those of the bulk, and the effects of the thermal spin fluctuations due to the excited magnons on the surface are markedly enhanced compared to that in the bulk region.

Slab calculations

Finally, to clarify the origin of the spin-polarized SS band exhibiting enhanced thermal spin fluctuation observed just below E_F, we performed the

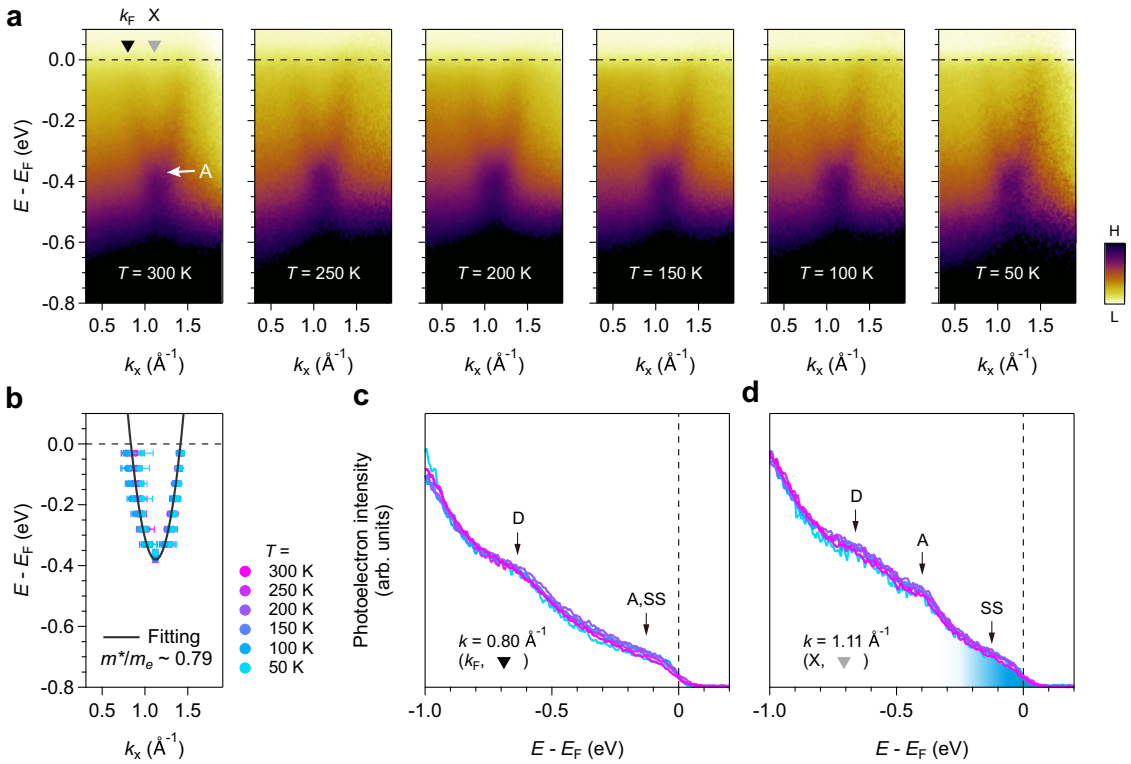

Fig. 2 | Temperature-dependent band structure. a Temperature-dependent ARPES images around X point recorded at 300, 250, 200, 150, 100, and 50 K on cooling. Colors show the photoelectron intensity. **b** Colored markers: peak fitting results by MDCs and EDCs of ARPES images shown in (**a**). Black curve: parabola fitting result of the colored markers. **c**, **d** Temperature-dependent EDCs at k_F ($k = 0.80$ Å^{-1}) and X point ($k = 1.11$ Å^{-1}). The measurement positions are indicated by black and gray inverted triangles in (**a**).

surface band calculations by considering a Co-terminated 17-atomic-layer slab with approximately a 20 Å vacuum layer. Figure 4a, b shows the calculated majority- and minority-spin bands along the $\bar{M}$–$\bar{\Gamma}$–$\bar{M}$ line (X–Γ–X line in the bulk Brillouin zone). Here, thick and thin bands represent the bulk and surface calculation results, respectively. For the majority-spin channel, many quantum-well-like bands, as well as relatively localized surface (resonance) bands, exist below E_F. We also find a mostly non-dispersive surface band around −0.1 eV within the bulk half-metallic gap in the minority-spin channel (black arrow). Such localized surface states might correspond to the experimentally observed band SS and collapse the half-metallicity on the surface. Note that the (001)-oriented Co_2MnSi crystal ideally has two nonequivalent surfaces, with either Co- or MnSi-terminations. However, the ARPES results were well reproduced by the slab calculations for the Co-termination rather than that for the MnSi-termination. The calculated bands for the MnSi-termination are shown in the Supplementary Information.

To identify the element-specific depth profiles, we calculated the layer-resolved Co and Mn local DOS (LDOS) projected onto each atomic sphere (Fig. 4c, d). The position of the atomic layer is indicated in Fig. 4e. For example, the first and fifth Co layers are located at the topmost surface and the inner position in our slab model, respectively. Through the depth-resolved calculations, we found that the LDOS of the topmost layer shows a unique and distinctive DOS compared to those of the deeper layers. Specifically, the first Co layer forms a large DOS with a minority-spin character at E_F. The first Mn layer, which is located just below the first Co layer, has two prominent peaks with a majority-spin character around −0.2 and −0.6 eV and the flat DOS with a minority-spin character in the half-metallic gap region. On the other hand, as the layer number becomes larger, both Co and Mn LDOS approach to a bulk-like DOS shape. These results signify that the topmost Co and Mn atoms play an important role in the loss of the half-metallicity and in forming the in-gap surface state. Considering the angstrom-order short inelastic mean free path of VUV-ARPES and SARPES measurements, the experimentally observed mostly non-dispersive and spin-polarized SS band showing high α value (enhanced thermal spin fluctuation) might be attributed to the topmost Co and Mn atoms. Our findings are consistent with previous theoretical work, which predicted that the exchange constant of the topmost atom of Co_2MnSi is markedly weakened compared with that of the bulk[23]. Thus, we conclude that the temperature-dependent spin-depolarization of Co_2MnSi films observed by surface-sensitive VUV-SARPES originates from surface magnon excitation.

Conclusion

In summary, we have experimentally investigated the temperature evolution of the surface band structures of the ferromagnetic Co_2MnSi Heusler alloy film using high-resolution VUV-SARPES. We directly observed the spin-polarized bands around E_F and determined the band-structure-related parameters such as the Fermi momentum, Fermi velocity, effective mass, and spin-polarization. We also revealed that spin-polarization markedly increases with decreasing temperature, and the temperature-dependent behavior of spin-polarization can be described by the thermally excited magnon model even well below T_C. By comparison with bulk-sensitive measurements, we conclude that the thermal spin fluctuation is markedly enhanced on its surface. Our findings pave the way for developing and improving spintronic device applications using half-metallic ferromagnetic Heusler thin films.

Methods

Thin film growth and characterization

Epitaxial (001)-oriented Co_2MnSi thin film was fabricated by the magnetron sputtering method using a polycrystalline target. The base pressure of the deposition chamber was $\sim 2 \times 10^{-7}$ Pa. A 30-nm-thick Co_2MnSi film was deposited on a MgO(001) single crystalline substrate with buffer layers of Cr (10 nm) and Ag (100 nm) at 600 °C. To avoid the formation of Co-Mn

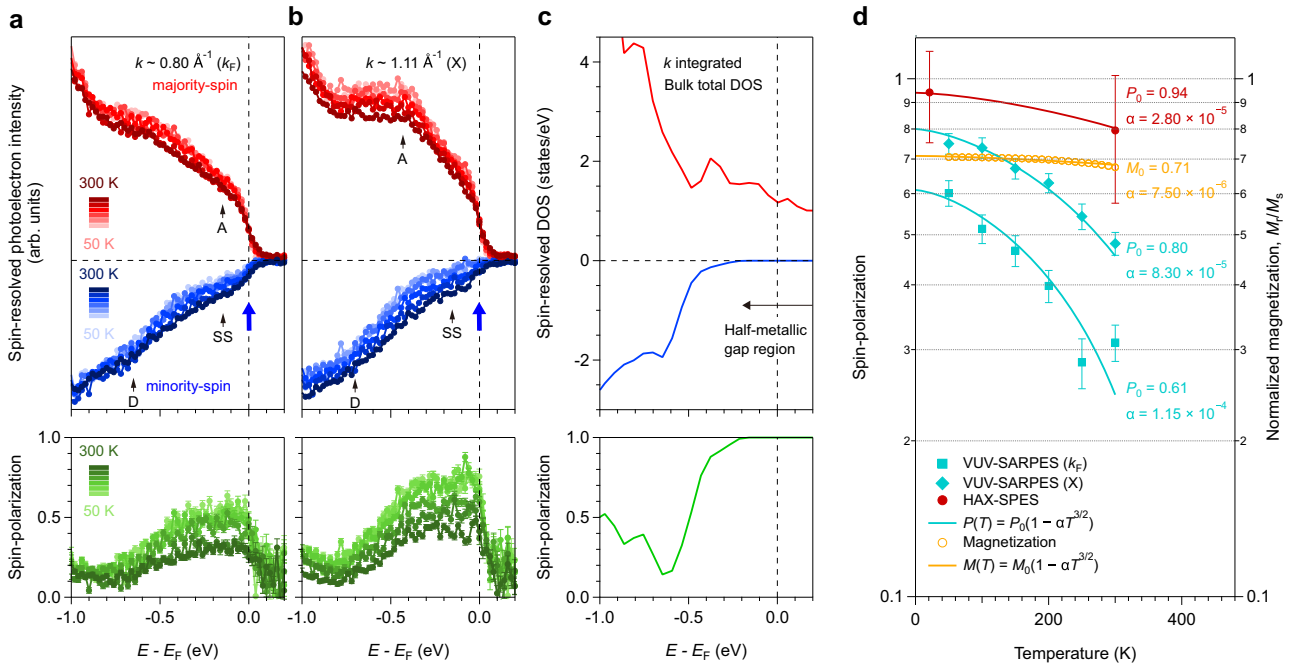

Fig. 3 | Temperature-dependent spin-polarization. a, **b** Temperature-dependent spin-resolved photoelectron intensities (upper) and spin-polarization (lower) around k_F (**a**) and X point (**b**) acquired in a range from 300 to 50 K. The measurement momenta are indicated by black and gray inverted triangles in Fig. 2a. **c** Calculated spin-resolved DOS (upper) and spin-polarization (lower) of bulk Co_2MnSi. **d** Temperature-dependent spin-polarization at E_F observed by surface-sensitive VUV-SARPES (this study, blue-green) and bulk-sensitive HAX-SPES[32] (red). Temperature-dependent M_r is also displayed (this study, orange). M_r is normalized by M_s at each temperature (see Fig. 1c). Colored solid curves represent the fitting results based on the thermal spin-wave excitation model. All error bars represent standard deviation.

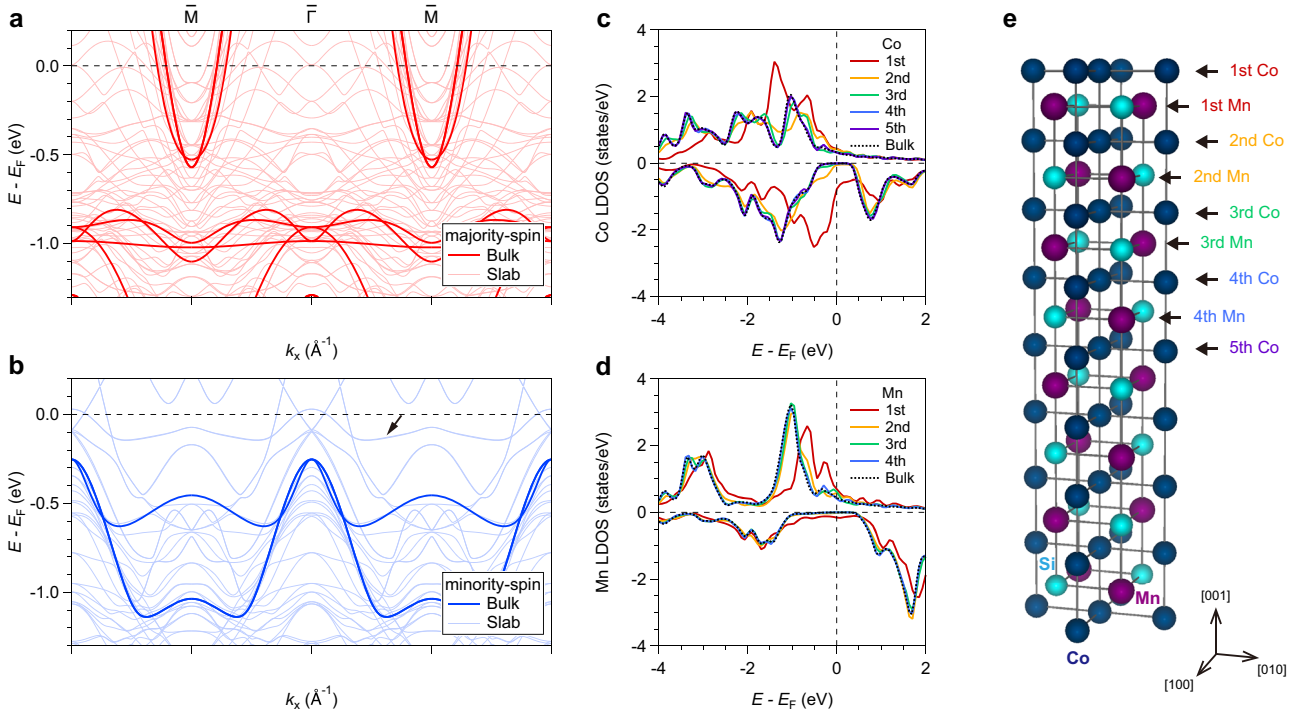

Fig. 4 | Calculated electronic structure of Co-terminated Co_2MnSi(001) surface. a, **b** Calculated band structures in majority- (**a**) and minority-spin channel (**b**). Thick and thin bands represent the bulk band along the X–Γ–X line and slab calculation results along the M̄–Γ̄–M̄ line, respectively. The black arrow indicates the weakly dispersive surface states. **c**, **d** Calculated atomic layer-dependent LDOS for the top five Co layers (**c**) and the top four Mn layers (**d**). Calculated bulk LDOS is also displayed. **e** Co-terminated Co_2MnSi crystal structure with 17 atomic layers. The atom positions for the LDOS plot (**c**, **d**) are indicated by the arrows.

antisites, we grew a slightly Mn-rich Co_2MnSi film. The grown film was transferred from the magnetron sputtering chamber to the SARPES chamber using a portable suitcase chamber ($<1 \times 10^{-6}$ Pa) to prevent oxidation. After SARPES measurements, the structural and magnetic properties of the sample were measured. The crystal structure and the surface morphology were determined by XRD with a Cu Kα X-ray source and AFM, respectively. The atomic composition was confirmed by wavelength dispersive X-ray fluorescence analysis to be $Co_{1.92}Mn_{1.26}Si_{0.82}$. The magnetic properties of the Co_2MnSi film were measured with a superconducting quantum interference device-vibrating sample magnetometer at various temperatures.

Spin-resolved and angle-resolved photoelectron spectroscopy

ARPES and SARPES measurements were performed at the ESPRESSO endstation (BL-9B) at the Research Institute for Synchrotron Radiation Science of Hiroshima University[41,42]. Spin-polarized photoelectrons were acquired using a hemispherical electron analyzer (R4000-WAL, Scienta-Omicron) equipped with VLEED-type spin detectors. The experimental geometry is shown in the Supplementary Information. The energy and angular resolutions for ARPES (SARPES) were set to 40 meV (52 meV) and $\pm 0.3°$ ($\pm 1.5°$), respectively. The effective Sherman function was 0.25. The sample was annealed at 550°C for 30 min in the preparation chamber and then magnetized along the [110] direction using a permanent magnet (~0.1 T) at room temperature prior to the ARPES and SARPES measurements.

Theoretical calculations

First-principles calculations based on density-functional theory implemented in the Vienna ab initio simulation program (VASP)[43] were performed on the $L2_1$-ordered Co_2MnSi. We adopted the generalized gradient approximation[44] for the exchange-correlation energy and employed the projected augmented wave pseudopotential[45,46] to treat the effect of core electrons properly. The lattice constant of the cubic unit cell was set to the experimentally determined value of 5.640 Å. For the bulk band calculation, the Brillouin zone integration was performed with $25 \times 25 \times 25$ k points. For the slab calculation, we considered 17 atomic layer supercell (4 unit cells) with ~20 Å vacuum layer. All the atomic positions are relaxed in the supercell, and the k-point number in the self-consistent-field calculation was chosen as $15 \times 15 \times 3$.

Data availability

The data presented in this paper are available from the authors upon reasonable request.

Received: 17 May 2024; Accepted: 19 December 2024;
Published online: 04 January 2025

References

1. Graf, T., Felser, C. & Parkin, S. S. P. Simple rules for the understanding of Heusler compounds. *Prog. Solid State Chem.* **39**, 1 (2011).
2. Felser, C. & Hirohata, A. *Heusler Alloys: Properties, Growth, Applications*. (Springer International Publishing, 2016).
3. Kojima, T., Kameoka, S., Fujii, S., Ueda, S. & Tsai, A. P. Catalysis-tunable Heusler alloys in selective hydrogenation of alkynes: a new potential for old materials. *Sci. Adv.* **4**, eaat6063 (2018).
4. Belopolski, I. et al. Discovery of topological Weyl fermion lines and drumhead surface states in a room temperature magnet. *Science* **365**, 1278 (2019).
5. Sumida, K. et al. Spin-polarized Weyl cones and giant anomalous Nernst effect in ferromagnetic Heusler films. *Commun. Mater.* **1**, 89 (2020).
6. Elphick, K. et al. Heusler alloys for spintronic devices: review on recent development and future perspectives. *Sci. Technol. Adv. Mater.* **22**, 236 (2021).
7. Kubler, J., William, A. R. & Sommers, C. B. Formation and coupling of magnetic moments in Heusler alloys. *Phys. Rev. B* **28**, 1745 (1983).
8. Ishida, S., Asano, S. & Ishida, J. Bandstructures and hyperfine fields of Heusler alloys. *J. Phys. Soc. Jpn* **53**, 2718 (1984).
9. Fujii, S., Sugimura, S. & Asano, S. Hyperfine fields and electronic structures of the Heusler alloys Co_2MnX (X=Al, Ga, Si, Ge, Sn). *J. Phys.* **2**, 8583 (1990).
10. Galanakis, I., Dederichs, P. H. & Papanikolaou, N. Slater-Pauling behavior and origin of the half-metallicity of the full-Heusler alloys. *Phys. Rev. B* **66**, 174429 (2002).
11. Sakuraba, Y. et al. Huge spin-polarization of $L2_1$-ordered Co_2MnSi epitaxial Heusler alloy film. *Jpn J. Appl. Phys.* **44**, L1100 (2005).
12. Sakuraba, Y. et al. Giant tunneling magnetoresistance in Co_2MnSi/Al-O/Co_2MnSi magnetic tunnel junctions. *Appl. Phys. Lett.* **88**, 192508 (2006).
13. Yakushiji, K. et al. Current-perpendicular-to-plane magnetoresistance in epitaxial Co_2MnSi/Cr/Co_2MnSi trilayers. *Appl. Phys. Lett.* **88**, 222504 (2006).
14. Ishikawa, T., Hakamata, S., Matsuda, K., Uemura, T. & Yamamoto, M. Fabrication of fully epitaxial Co_2MnSi/MgO/Co_2MnSi magnetic tunnel junctions. *J. Appl. Phys.* **103**, 07A919 (2008).
15. Iwase, T. et al. Large interface spin-asymmetry and magnetoresistance in fully epitaxial Co_2MnSi/Ag/Co_2MnSi current-perpendicular-to-plane magnetoresistive devices. *Appl. Phys. Express* **2**, 063003 (2009).
16. Sakuraba, Y. et al. Mechanism of large magnetoresistance in Co_2MnSi/Ag/Co_2MnSi devices with current perpendicular to the plane. *Phys. Rev. B* **82**, 094444 (2010).
17. Hu, B. et al. Temperature dependence of spin-dependent tunneling conductance of magnetic tunnel junctions with half-metallic Co_2MnSi electrodes. *Phys. Rev. B* **94**, 094428 (2016).
18. Chioncel, L. et al. Nonquasiparticle states in Co_2MnSi evidenced through magnetic tunnel junction spectroscopy measurements. *Phys. Rev. Lett.* **100**, 086402 (2008).
19. Mavropoulos, P., Lezaic, M. & Blugel, S. Half-metallic ferromagnets for magnetic tunnel junctions by *ab initio* calculations. *Phys. Rev. B* **72**, 174428 (2005).
20. Masuda, K., Tadano, T. & Miura, Y. Crucial role of interfacial *s-d* exchange interaction in the temperature dependence of tunnel magnetoresistance. *Phys. Rev. B* **104**, L180403 (2021).
21. Miura, Y., Uchida, H., Oba, Y., Abe, K. & Shirai, M. Half-metallic interface and coherent tunneling in Co_2YZ/MgO/Co_2YZ (YZ = MnSi, CrAl) magnetic tunnel junctions: a first-principles study. *Phys. Rev. B* **78**, 064416 (2008).
22. Miura, Y., Abe, K. & Shirai, M. Effects of interfacial noncollinear magnetic structures on spin-dependent conductance in Co_2MnSi/MgO/Co_2MnSi magnetic tunnel junctions: a first-principles study. *Phys. Rev. B* **83**, 214411 (2011).
23. Sakuma, A., Toga, Y. & Tsuchiura, H. Theoretical study on the stability of magnetic structures in the surface and interfaces of Heusler alloys, Co_2MnAl and Co_2MnSi. *J. Appl. Phys.* **105**, 07C910 (2009).
24. Shinya, H. et al. First-principles calculations of finite temperature electronic structures and transport properties of Heusler alloy Co_2MnSi. *Appl. Phys. Lett.* **117**, 042402 (2020).
25. Nawa, K. et al. Temperature-dependent spin polarization of Heusler Co_2MnSi from the disordered local-moment approach: effects of atomic disordering and nonstoichiometry. *Phys. Rev. B* **102**, 054424 (2020).
26. Wang, W. H. et al. Magnetic properties and spin polarization of Co_2MnSi Heusler alloy thin films epitaxially grown on GaAs(001). *Phys. Rev. B* **71**, 144416 (2005).
27. Wustenberg, J.-P. et al. Surface spin polarization of the nonstoichiometric Heusler alloy Co_2MnSi. *Phys. Rev. B* **85**, 064407 (2012).
28. Jourdan, M. et al. Direct observation of half-metallicity in the Heusler compound Co_2MnSi. *Nat. Commun.* **5**, 3974 (2014).
29. Andrieu, S. et al. Direct evidence for minority spin gap in the Co_2MnSi Heusler compound. *Phys. Rev. B* **93**, 094417 (2016).

30. Guillemard, C. et al. Ultralow magnetic damping in Co_2Mn-based Heusler compounds: Promising materials for spintronics. *Phys. Rev. Appl.* **11**, 064009 (2019).
31. Guillemard, C. et al. Engineering $Co_2MnAl_xSi_{1-x}$ Heusler compounds as a model system to correlate spin polarization, intrinsic Gilbert damping, and ultrafast demagnetization. *Adv. Mater.* **32**, 1908357 (2020).
32. Ueda, S., Miura, Y., Fujita, Y. & Sakuraba, Y. Direct probing of temperature-independent bulk half-metallicity in Co_2MnSi by spin-resolved hard x-ray photoemission. *Phys. Rev. B* **106**, 075101 (2022).
33. Shang, C. H., Nowak, J., Jansen, R. & Moodera, J. S. Temperature dependence of magnetoresistance and surface magnetization in ferromagnetic tunnel junctions. *Phys. Rev. B* **93**, R2917 (1998).
34. Raphael, M. P. et al. Magnetic, structural, and transport properties of thin film and single crystal Co_2MnSi. *Appl. Phys. Lett.* **79**, 4396 (2001).
35. Kijima, H. et al. Epitaxial growth of full-Heusler alloy Co_2MnSi thin films on MgO-buffered MgO substrates. *IEEE Trans. Magn.* **42**, 2688 (2006).
36. Stephan, R., Dulot, F., Mehdaoui, A., Berling, D. & Wetzel, P. Molecular-beam epitaxy of Co_2MnSi Heusler alloy thin films epitaxially grown on Si(001). *J. Magn. Magn. Mater.* **320**, 1043 (2008).
37. Miyamoto, K. et al. Absence of temperature dependence of the valence-band spectrum of Co_2MnSi. *Phys. Rev. B* **79**, 100405(R) (2009).
38. Mauri, D., Scholl, D., Siegmann, H. C. & Kay, E. Observation of the exchange interaction at the surface of a ferromagnet. *Phys. Rev. Lett.* **61**, 758 (1988).
39. Scholl, D. et al. Exchange interactions at the surface of a ferromagnet. *Phys. Rev. B* **43**, 13309 (1991).
40. Seah, M. P. & Dench, W. A. Quantitative electron spectroscopy of surfaces: a standard data base for electron inelastic mean free paths in solids. *Surf. Interface Anal.* **1**, 2 (1979).
41. Okuda, T. et al. Efficient spin resolved spectroscopy observation machine at Hiroshima Synchrotron Radiation Center. *Rev. Sci. Instrum.* **82**, 103302 (2011).
42. Okuda, T., Miyamoto, K., Kimura, A., Namatame, H. & Taniguchi, M. A double VLEED spin detector for high-resolution three dimensional spin vectorial analysis of anisotropic Rashba spin splitting. *J. Electron Spectrosc. Relat. Phenom.* **201**, 23 (2015).
43. Kresse, G. & Furthmuller, J. Efficient iterative schemes for *ab initio* total-energy calculations using a plane-wave basis set. *Phys. Rev. B* **54**, 11169 (1996).
44. Perdew, J. P., Burke, K. & Ernzerhof, M. Generalized gradient approximation made simple. *Phys. Rev. Lett.* **77**, 3865 (1996).
45. Blochl, P. E. Projector augmented-wave method. *Phys. Rev. B* **50**, 17953 (1994).
46. Kresse, G. & Joubert, D. From ultrasoft pseudopotentials to the projector augmented-wave method. *Phys. Rev. B* **59**, 1758 (1999).

Acknowledgements

We thank Y. Takeda, K. Nakanishi, and K. Ohwada for their technical support. The SARPES measurements were performed with the approval of the Proposal Assessing Committee of the Research Institute for Synchrotron Radiation Science of Hiroshima University (Proposals Nos. 18BG038, 18BG040, and 21BG009). The slab calculations in this work were performed on the Numerical Materials Simulator at the National Institute for Materials Science. This work was financially supported by KAKENHI (Nos. 17H06152, 17H06138, 18H01954, 18H03683, 20H00347, 21K14540, 23K03933, 24K17614, and 24K21533).

Author contributions

K.S. and M.K. contributed equally to this work. K.S., M.K., and T.K. performed the SARPES experiments with the assistance of K.Mi and T.O. Y.S. and K.G. synthesized the thin-film sample. K. Ma and Y.M. performed the theoretical calculations. K.S. and M.K. analyzed data. K.S. wrote the paper with inputs from all authors. K.H. and A.K. supervised the work.

Competing interests

All authors declare no competing interests.

Additional information

Supplementary information The online version contains supplementary material available at https://doi.org/10.1038/s42005-024-01918-w.

Correspondence and requests for materials should be addressed to Kazuki Sumida or Akio Kimura.

Peer review information *Communications Physics* thanks Madhab Neupane and the other, anonymous, reviewer(s) for their contribution to the peer review of this work. A peer review file is available.